Influence of Pore Structure on Drying Kinetics: A Pore Network Study

Thomas Metzger, Anton Irawan, and Evangelos Tsotsas
Thermal Process Engineering, Otto-von-Guericke-University, P.O. 4120, 39016 Magdeburg, Germany

DOI 10.1002/aic.11307

A pore network model for convective drying is applied to investigate the influence of structure on drying behavior. The isothermal drying model is based on the work of Prat, and uses invasion percolation concepts, neglecting any viscous or gravitational effects. Pore structures of different pore-size distribution and coordination number are studied in two- and three-dimensions. Results are given as phase distributions or moisture profiles during drying, as well as drying rate curves. Significant differences in drying kinetics are reported for a variation in coordination number of monomodal networks. Bimodal pore structures can produce dramatically higher drying rates, but only for certain spatial correlations of small and large pores. Finally, influence of product thickness and importance of boundary layer modeling are addressed. © 2007 American Institute of Chemical Engineers *AIChE J,* 53: 3029–3041, 2007

Keywords: drying rate, phase distributions, porous media, pore-size distribution, coordination number

Introduction

Drying kinetics of porous media depend on two classes of parameters: the first describes drying conditions, the second the material itself. In convective drying, the initial drying rate of a liquid-saturated material is only given by temperature, humidity and velocity of drying air and outer geometry of the porous body; this rate is identical to the evaporation rate of a liquid surface, and structural properties of the material will not influence it. Pore structure will, however, determine for how long this initial rate can be maintained (first drying period), and how drying rate will decrease during the so-called second drying period. Then, heat and mass transfer are controlled by inner resistances. Theoretical description of drying behavior is a challenging task, but can be of great benefit for optimal process design and product innovation.

One way to describe the transport phenomena in partially saturated porous media is by a continuous model based on volume-averaging;[1] this model employs effective parameters for thermodynamic equilibrium, such as capillary pressure and sorption isotherm, and for transport, such as absolute and relative permeabilities, diffusivity and thermal conductivity. All these parameters are functions of saturation and do strongly depend on pore structure. They may either be measured by independent experiments, or modeled from more fundamental structural information.

Discrete models of drying use a simplified geometry to represent the real pore space, such as a bundle of capillaries or a network of pores, and describe transport phenomena at the pore level. Depending on the complexity of the model, more or less structural information can be implemented. A bundle-of-capillaries geometry can only account for pore-size distribution, whereas pore networks can also account for spatial correlations of pore size, connectivity of pores, or pore shape. Such representative pore spaces can serve either to simulate the drying process directly or to compute effective parameter functions to be used in a continuous model. In this way, the influence of pore-size distribution on drying behavior has recently been studied for a bundle of capillaries, directly by a discrete model,[2] as well as via effective parameters in a continuous model.[3,4] This work aims to start similar investigations with the more versatile tool of pore networks.

Correspondence concerning this article should be addressed to T. Metzger at thomas.metzger@ovgu.de.

Since the early 1990s, pore network modeling has become increasingly popular in the field of drying. In most studies, only mass transfer is modeled, mainly as vapor diffusion in the gas phase and capillary flow in the liquid phase. The seemingly first work by Nowicki et al.[5] represents pore space by a network of biconical throats; liquid flow is subject to viscous effects. Drying is simulated for a representative network in order to compute effective parameters as used in the continuous approach.

One year later, Prat[6] proposed a network drying model with cylindrical pore throats, which is based on an invasion percolation algorithm; gravity is modeled, but viscous effects are neglected. This model is applied at the sample scale; accordingly, results are reported as phase distributions in the porous structure. Recently, an algorithm to include viscous effects in the liquid has been proposed for this model.[7,8]

A third network model has been presented by Yiotis et al.[9] who investigated drying of porous rock by purging gas through an adjacent fracture. The network is built from spherical pores that contain all pore volume; the connecting cylindrical throats only act as conductors and capillary barriers. Viscous effects are accounted for in both gas and liquid, but mainly play a role in the gas. Simulation results are presented as phase patterns and drying curves.

The latter two approaches have recently been extended to film effects,[10,11] which can produce a first drying period if pores have corners and wetting conditions are favorable. Drying experiments with etched networks could confirm the simulated phase distributions[12] and show the important role of film flow for drying rates.[13]

Due to computational limitations, three-dimensional (3-D) simulations are still rare and have only been presented for basic model versions, i.e., without viscous or film effects, to realistically analyze the drying curve with respect to percolation phenomena, such as disconnected cluster formation and breakthrough.[14,15] The role of lateral vapor transfer in the gas-side boundary layer in producing a first drying period has been pointed out in this context (see also Ref. 16).

Further investigations with model variants include evaporation of binary liquids[17] and influence of imposed thermal gradients;[18,19] only recently a network model accounting for heat transfer in convective drying has been proposed.[20]

Phase distributions during drying have been analyzed by invasion percolation concepts as proposed by Ref. 21 and Ref. 22; viscous effects will always stabilize the drying front, whereas gravity and temperature gradients can be stabilizing or destabilizing depending on their orientation with respect to the open side of the network. In any of these cases, the width of pore-size distribution plays a significant role since it defines the available pressure differences for capillary pumping.

This brief review shows that, step by step, more and more effects have been included into pore network models, so that an assessment of the continuous model is within reach. In this context, the network approach is seen as the more fundamental description. A major task is to investigate the range of validity of continuous concepts, e.g., the generalized Darcy law for two-phase flow might well describe a stabilized invasion, whereas it is difficult to imagine how it shall describe mass transfer near a percolation threshold, or when the liquid phase has split up into many disconnected clusters. If equivalence between discrete and continuous approach can be shown, representative pore networks may indeed serve to compute effective parameters. Furthermore, the stepwise approach illustrates the power of network modeling: the macroscopic effect of any pore-level transport phenomenon can be studied individually.

Besides this investigation of effects, network modeling can help to analyze the influence of pore space geometry and topology on drying behavior. The effect of pore shape has been studied with model versions accounting for corner films.[23,11] Investigation of the influence of pore-size distribution and pore structure has only been started recently by the authors.[24,16,8] Previously, only large-scale inhomogeneities of the porous medium were considered as structural effects influencing phase distributions.[25]

The objective of this work is to systematically study the influence of pore structure on drying behavior. First, the drying model of Prat is recalled, relevant transport phenomena in network and adjacent boundary layer are pointed out and aspects of the drying algorithm explained. In the next step, this model is applied to regular square pore networks (2-D) with mono- and bimodal pore-size distributions; several pore structures are studied for the same bimodal distribution by varying the spatial correlation of macropores. Simulation results are discussed on the basis of drying rate curves and liquid phase distributions. It is found that pore-size distribution and pore structure have a big effect on drying kinetics.

For further investigation, the Monte-Carlo method is introduced as an appropriate tool to compare results for different structural classes. With this method, drying behavior of regular 2-D networks of different coordination number is compared. A significant effect of this structural property on drying kinetics can be shown. All these 2-D simulations show that the major effect of structure on drying kinetics is by the disintegration of the liquid phase into separate clusters (resulting in interruption of capillary flow), which depends on coordination number and spatial correlation of pore sizes.

In the last section, the computationally more demanding simulation of three-dimensional networks is addressed, again by comparing drying behavior (drying curves and moisture profiles) for different pore-size distributions and coordination numbers. These Monte-Carlo simulations confirm the previous 2-D findings. Finally, the influence of porous medium thickness is studied, and the importance of boundary layer modeling is demonstrated for the 3-D geometry.

Pore Network Drying Model

Throughout this article, we consider the drying process as isothermal which is a reasonable approximation only for moderate drying conditions. Pore size is always chosen big enough so that viscosity, Kelvin and Knudsen effects are negligible; film effects are not relevant for the chosen cylindrical geometry of pore throats. Gravity could be easily modeled, but is deliberately set to zero to simplify the analysis of phenomena. Furthermore, we restrict our investigations to capillary porous media and model only free water, not adsorbed water. These strong assumptions are valid only for a limited range of materials and drying conditions, but such a restriction is justified since our major interest is in the role of structural influences; the use of a simple algorithm allows investigating the problem by the appropriate, but time-consuming Monte-Carlo method.

In this section, we discuss the main elements of the drying algorithm as introduced by Prat[6] pointing out recent developments; a more detailed description is given in Ref. 26.

Pore network and gas-side boundary layer

The porous medium is represented by a network of pore nodes (without volume) that are connected by cylindrical pore throats of random radius; the solid phase need not be modeled for isothermal conditions. We restrict ourselves to regular networks of constant coordination number, but go beyond previous work that used only square or cubic networks. In all simulations, the network is initially saturated with water; then, water is removed by convective drying through the top side of the network. In horizontal direction(s), periodic boundary conditions are applied; the network bottom is impermeable. Figure 1 shows part of a partially dried 2-D square network with mono-modal throat radius distribution. Because of the random spatial distribution, capillary flow from large to small throats and liquid cluster formation are random processes as well.

Throughout this article, we use normal number distributions to generate throat radii. Monomodal networks are characterized by mean and standard deviation of radius; for bi-modal distributions, the volume fraction of the two normal modes must additionally be given.

Drying rate depends on the liquid-phase distribution in the network and vapor diffusion through empty network regions and gas-side boundary layer. Traditionally, boundary-layer vapor transfer has been described for each surface pore by a mass-transfer coefficient β that can be obtained from dimensionless correlations. This will induce a sharp decrease in the drying rate as soon as the first surface throats dry out, leading to a drying rate roughly proportional to surface saturation. More recently, lateral vapor diffusion in the boundary layer is included into modeling[16,15] by extending the discrete network of pore nodes into the gas by boundary-layer thickness $s = \delta/\beta$ where δ is vapor diffusivity (see Figure 2). This phenomenon is seen as a major reason for the occurrence of an extended constant rate drying period.[27] Another explanation is by film flow in gas-filled throats that can transport liquid to the network surface and keep it sufficiently wet; but this effect is negligible for pores without corners.

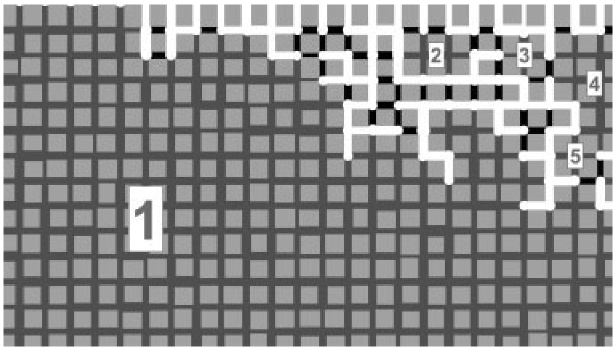

Figure 1. Part of pore network with monomodal throat-size distribution during convective drying by the top.

Empty throats are in white, liquid throats belonging to a cluster in dark gray (with respective cluster label), and single liquid throats in black.

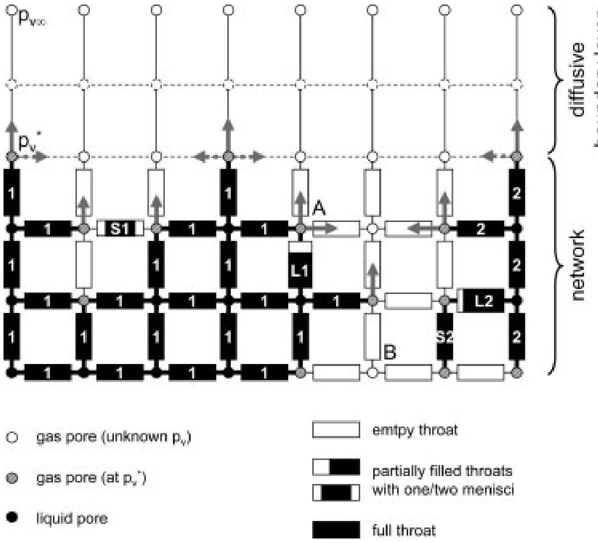

Figure 2. Example of a small partially dried pore network with discretized boundary layer to describe vapor transfer under convective drying conditions.

Boundary conditions for vapor diffusion are given, and resulting vapor flows are sketched at the liquid-gas interface (gray arrows), indicating the enhancement due to lateral diffusion in the boundary layer (dashed arrows). The liquid phase consists of two separate clusters, in either of which only the largest meniscus throat is emptying (L1 and L2), and two single throats (S1 and S2).

Vapor diffusion and capillary pumping

Since gas is the invading phase, it stays continuous, whereas the liquid typically splits up into numerous clusters. Mass transfer is controlled by vapor diffusion in the gas-filled part of the network and capillary pumping in liquid-filled regions. As capillary forces are assumed dominant over viscous forces, only the largest meniscus throat in a cluster will empty at a time, while water is pumped to all other meniscus throats at their respective evaporation rates, so that their menisci remain stationary. Local evaporation rates are computed from mass balances in the gas phase describing vapor diffusion as a quasi-steady process during the emptying of one throat

$$\sum_j \dot{M}_{v,ij} = \sum_j A_{ij} \frac{\delta}{L} \frac{p\tilde{M}_v}{\tilde{R}T} \cdot \ln\left(\frac{p - p_{v,i}}{p - p_{v,j}}\right) = 0 \tag{1}$$

The mass flow rate $\dot{M}_{v,ij}$ between two gas pores i and j, which are connected by an empty throat, is computed from its length L and cross-sectional area

$$A_{ij} = \begin{cases} \pi r_{ij}^2 & \text{in network} \\ L^2 & \text{in boundary layer} \end{cases}, \tag{2}$$

total pressure p, molar mass of vapor $\tilde{M}_v$, ideal gas constant R, absolute temperature T, and partial vapor pressures $p_{v,i}$ and $p_{v,j}$, respectively. Here, the logarithmic law describes combined vapor diffusion and (nonviscous) gas convection next to an evaporating liquid-gas interface. Boundary conditions to Eq. 1 are given by vapor pressure of drying air $p_{v\infty}$ at the far end of the boundary layer, and by assuming equilibrium vapor pressure p_v^* in pores next to a (partially) filled throat as indicated in Figure 2. There, an example is given of a small partially saturated network with two liquid clusters and two single liquid throats; evaporation is shown by gray arrows. If several menisci are neighbor to a pore (A), total vapor flow away from this pore is distributed to them according to their cross-sections in order to obtain local evaporation rates. Note that, in the depth of the network, whole gas regions (B) can be at equilibrium vapor pressure if surrounded by menisci (then nonevaporating). At any time, largest cluster menisci (L1 and L2), as well as single liquid throats (S1 and S2), are candidates for emptying. If ideal capillary pumping within each liquid cluster is assumed, timescale and order of invasion are only given by the respective cluster sums of local evaporation rates. (Individual clusters can be temporarily trapped, such as single liquid throat S2.) It, is, therefore, crucial to correctly track cluster affiliation of liquid throats during drying.

Cluster labeling

Initially, all throats are liquid-filled and belong to the same cluster (with label 1). In each time step, normally only one throat is emptied completely. If this throat belongs to a liquid cluster, a neighboring pore is also emptied leading to local separation of liquid throats by creation of new menisci. Therefore, we must check if the former throat members of this cluster are still connected by other capillary flow paths, or if the cluster has split up into separate clusters or single throats; in the latter case, relabeling is necessary. Since single throats do not participate in capillary flow, they get no throat label.

For relabeling, it is suitable to use a variant of the Hoshen-Kopelman algorithm[28,29] that starts at the emptied throat and is restricted to the corresponding cluster. The principle of the Hoshen-Kopelman algorithm is to scan the liquid throats one by one, check each time for already labeled neighboring liquid throats (connected by a liquid pore) and store information about labels that are found to be identical; only after scanning, labels will be corrected. If suitable stopping criteria are defined, the scanning can usually be limited to a small number of throats; this is explained in the following by help of Figure 3.

After emptying of the first surface throat (a), all liquid throats are still connected, but in the general case, this must be checked. The algorithm starts by attributing different labels to all former neighbors of the emptied throat (except single liquid throats). Then, consecutive generations of connected liquid neighbor throats are identified; these generations are labeled one after the other by the method of Hoshen-Kopelman, always attributing to a throat the minimum label already existing among direct neighbors, and storing information about identical labels. In our example, all new labels are in fact identical; the arrows indicate that this can be known after labeling the first generation. In general, several generations—and, in the worst case, all throats of the old cluster—must be scanned before the new cluster topology is known.

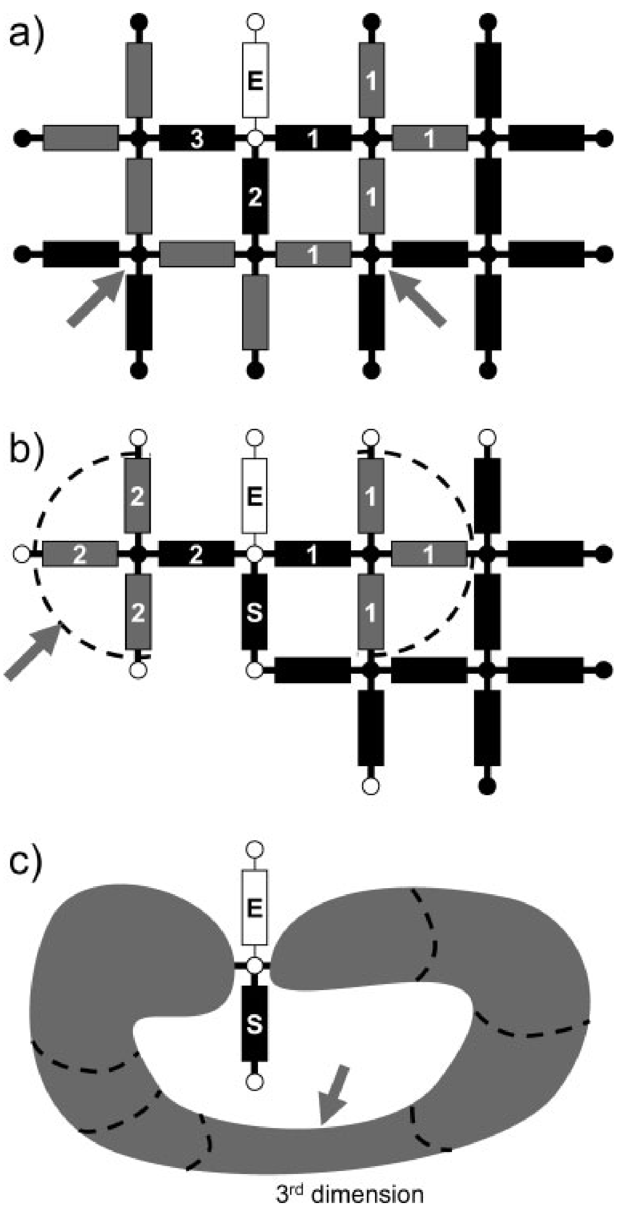

Figure 3. Relabeling of liquid throats adjacent to the throat emptied in last time step (E).

(a) After first throat is emptied, (b) situation as in upper righthand corner of Figure 1 and (c) case of a far-end connection of locally separated liquid regions (dashed lines indicate the successive generations scanned by the Hoshen-Kopelman algorithm, gray arrows show when the algorithm stops; more explanations are given in the text).

In practice, the algorithm may stop if all members of a new generation have been given the same label. This can have two reasons: either all except one of the newly created clusters are completely labeled or all remaining different clusters are found to be connected. An example of the first

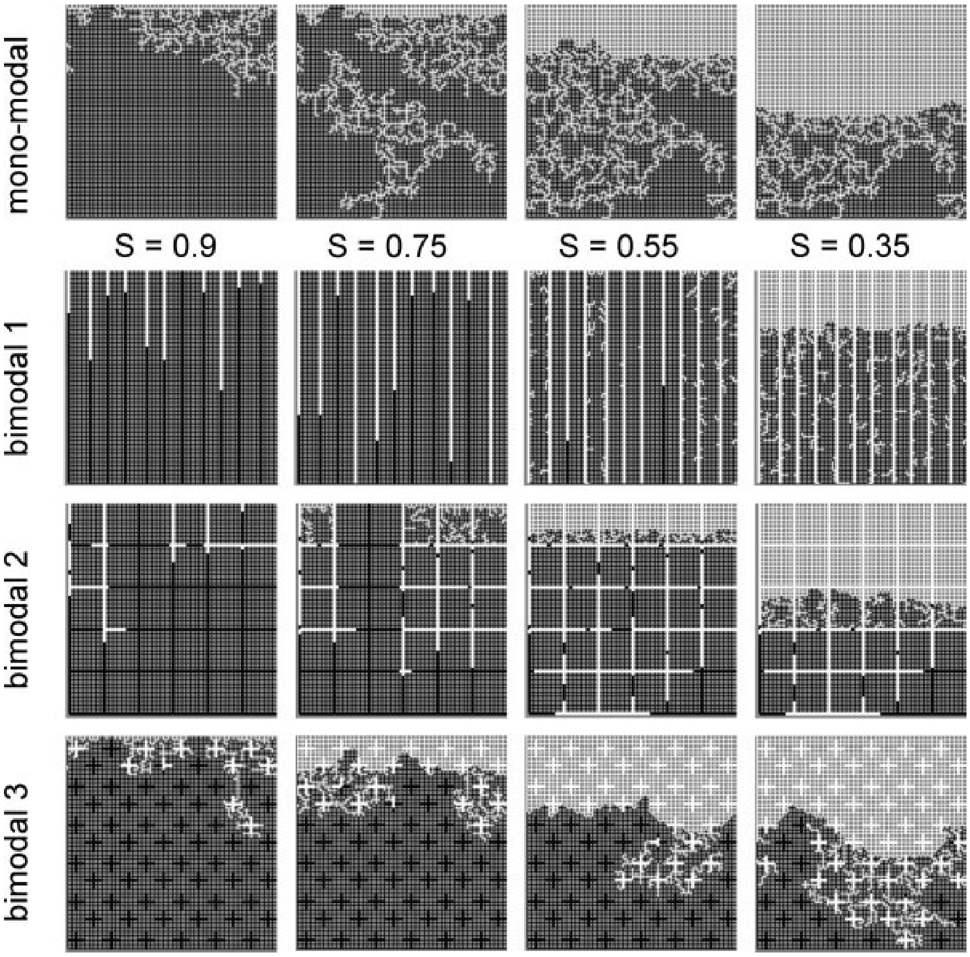

Figure 4. Drying behavior of 2-D networks with different pore structures: the first network has a monomodal pore-size distribution; the others have (almost) the same bimodal pore-size distribution, but different spatial distributions of small and large pores.

Phase distributions are shown for the indicated network saturations. (Liquid-filled throats are in black, empty throats in white.)

condition is shown in Figure 3b (situation as in the upper righthand corner of Figure 1) where cluster 2 has been scanned completely, and all further generations must, therefore, belong to cluster 1. The second condition has simple examples (such as in Figure 3a), but also nontrivial ones, such as liquid loops providing far-end connections occurring in three-dimensions (Figure 3c).

After scanning, these intermediate labels are updated, and only if new clusters have been created, the old cluster labels need to be shifted to accommodate them.

2-D Pore Networks

The aforementioned drying model is applied to a range of pore networks starting with 2-D ones. The first focus is on the role of macrothroats and their spatial correlation for drying behavior. Then, Monte-Carlo simulations are carried out, and an appropriate average presentation is chosen to compare behavior of different network classes, and to dispose of random variations between representatives of one class. With this method, we investigate the influence of coordination number for mono- and bimodal networks.

Influence of pore-size distribution

The first drying simulation is for a square 48 × 51 network, with throat length 500 μm and monomodal radius distribution of mean 40 μm, and standard deviation 2 μm. Drying air with zero moisture is at 20°C and atmospheric pressure; the boundary layer has 10 vertical nodes corresponding to a mass-transfer coefficient of 5.1 mm/s. The first line of Figure 4 shows phase distributions at the indicated network saturations (remember horizontal periodicity). The dimensionless drying rate curve is plotted in Figure 5 (solid line); the initial evaporation flux for a completely wet network surface is 0.32 kg/m^{2}h.

One can see that most of the surface rapidly dries out. This is accompanied by a drastic decrease in drying rate; a first drying period of constant rate is not observed. Due to an uncorrelated radius distribution, capillary pumping is a random process. Quasi-constant rate periods, random in start

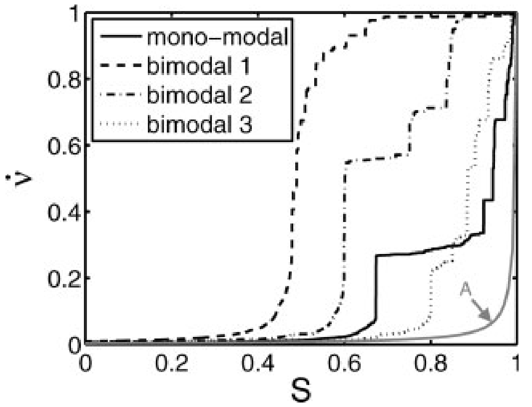

Figure 5. Normalized drying rate versus network saturation for the two-dimensional networks depicted in Figure 4.

The result for a sharply receding drying front, i.e., with no capillary pumping, is shown as curve A (for the monomodal network).

and duration, are observed, e.g., around network saturation S = 0.75, when inner-network throats are invaded, but near surface saturation, which controls mass transfer to bulk air, stays unchanged. When a zone of disconnected liquid clusters has formed, capillary pumping looses its importance and surface dries out completely (for 2-D simulations, this zone does not always span the whole network). The disconnected clusters dry out one by one, with a receding evaporation front. Soon we will see that in networks with a bimodal pore-size distribution, capillary flow can significantly enhance drying rates; but even in the unfavorable monomodal case, capillary pumping plays an important role as shows a comparison with the simulation with immobile water — and, therefore, a sharp drying front (see solid line in Figure 5 in contrast to curve A). A systematic investigation of this capillary enhancement effect has recently been presented by Chapuis and Prat.[30]

Many real porous media have a bimodal pore-size distribution; therefore, corresponding networks are generated by rescaling some throat radii to 100 ± 5 μm. As can be seen from Figure 4, these macro throats are spatially correlated in three different ways, as:

1. long channels perpendicular to network surface, so that the two "phases" of micropores and macropores are continuous (note that strict continuity cannot be achieved in 2-D);
2. long channels in both space directions, so that only the macropore phase is continuous, and we obtain a simple representation of an agglomerate of microporous particles;
3. regularly distributed small clusters—representing isolated "macro pores"—so that only micropores form a continuous phase.

All three structures have about the same volume fraction of macropores (0.447, 0.442 and 0.436, respectively); hence, their macroscopic properties porosity and pore-size distribution are similar. Their drying behavior under the same drying conditions as for the monomodal network is presented in Figures 4 and 5.

For the *first* structure, a long first drying period is observed during which the macrochannels empty, and liquid is pumped to the surface by the microthroats. The initial drying rate is maintained because of a good spatial distribution of wet surface throats, and lateral vapor transfer in the boundary layer. When almost all macrothroats are empty, disconnected clusters of microthroats develop (at S = 0.55) leading to drying out of whole surface regions and a drop in drying rate (see Figure 5). When no liquid is left in macrochannels, preferential capillary pumping stops and eventually disconnected clusters evaporate with a receding front.

The examples of the other two pore structures show that both micro- and macropores must constitute continuous phases for efficient drying. In the *second* bimodal structure, random emptying of horizontal macrochannels stops capillary flow to whole surface regions at an early stage ($S \geq 0.75$ in Figure 4), resulting in a short first drying period ($S > 0.9$ in Figure 5). In fact, the grid of macrochannels favors formation of clusters, which have small size and contain only microthroats so that capillary pumping plays a minor role, and the network dries out more or less layer by layer ($S \leq 0.55$ in Figure 4). The random disconnection and drying out of microporous regions is indeed quite similar to that of single throats in the monomodal network, only the respective length scales and timescales are larger.

Drying behavior of the *third* bimodal network structure is still closer to the monomodal case: here the randomness of throat emptying is only overruled for a short time when the gas-liquid interface reaches a macropore which is then first emptied completely (S = 0.9 in Figure 4). The presence of macrothroats does not dramatically influence drying efficiency (compare solid line and dotted line in Figure 5) since capillary pumping remains a random effect.

In conclusion, it shall be stressed that pore-size distribution does not sufficiently characterize a porous medium with respect to its drying behavior, but that spatial correlations of pore size are crucial: bimodal structures with unfavorable (or none at all) spatial correlation will behave similarly as monomodal ones. For the presented model, width of pore-size distribution plays a minor role: in the absence of pressure or temperature gradients, invasion order is dominated by relative size differences; and absolute throat size mainly affects evaporation rates. If gravitational, viscous or thermal effects are modeled, their influence will typically be significant when throats of similar size compete for liquid,[19] i.e., for monomodal networks or for bimodal networks at low saturations.

Monte-Carlo simulations

Previously, only one representative of each network structure was discussed. Naturally, the randomness of network generation will reflect in drying behavior, and different representatives of one class may have quite different drying curves. By performing 100 Monte-Carlo simulations per class, and looking at average behavior and random distributions, we will now assess this randomness to find out characteristic features of each class. The randomness of drying behavior for square monomodal networks has recently been studied by looking at the distributions of drying curves (saturation over time) and drying times.[30] The drying time distri-

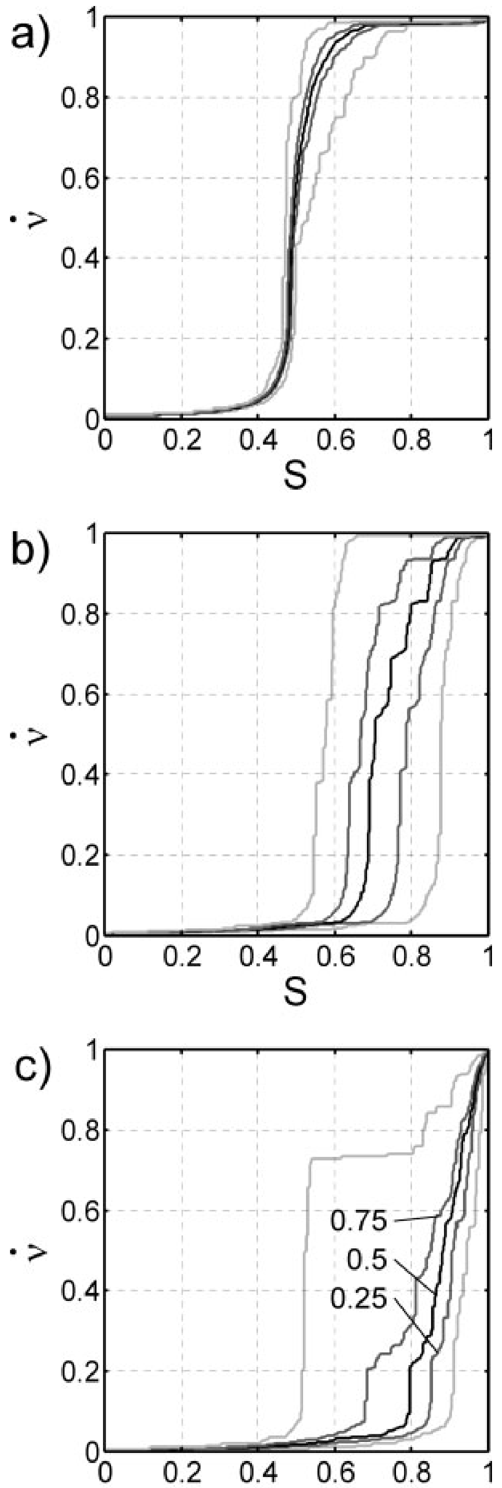

Figure 6. Drying rate curves for 2-D bimodal networks.

Normalized drying rate is plotted vs. network saturation (at 0.25 levels of cumulative distribution for 100 MC runs): (a) structure 1, (b) structure 2, and (c) structure 3. For representatives of these structures refer to Figure 4.

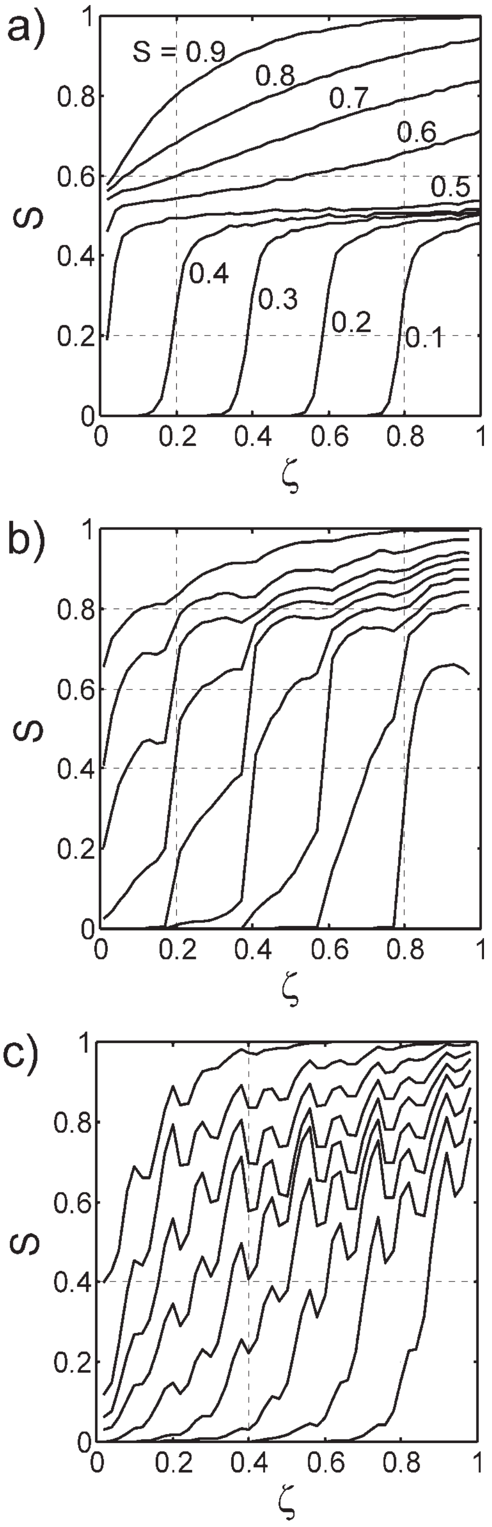

Figure 7. Saturation profiles during drying for 2-D bimodal networks.

Slice-averaged saturation is plotted vs. normalized network depth ζ as the average of 100 MC runs, for multiples of 0.1 in network saturation: (a) structure 1, (b) structure 2, and (c) structure 3. For representatives of these structures see Figure 4.

bution was found to be nearly Gaussian; dependencies on network size, and the role of film effects were also investigated. In this work, we inspect drying rate curves (drying

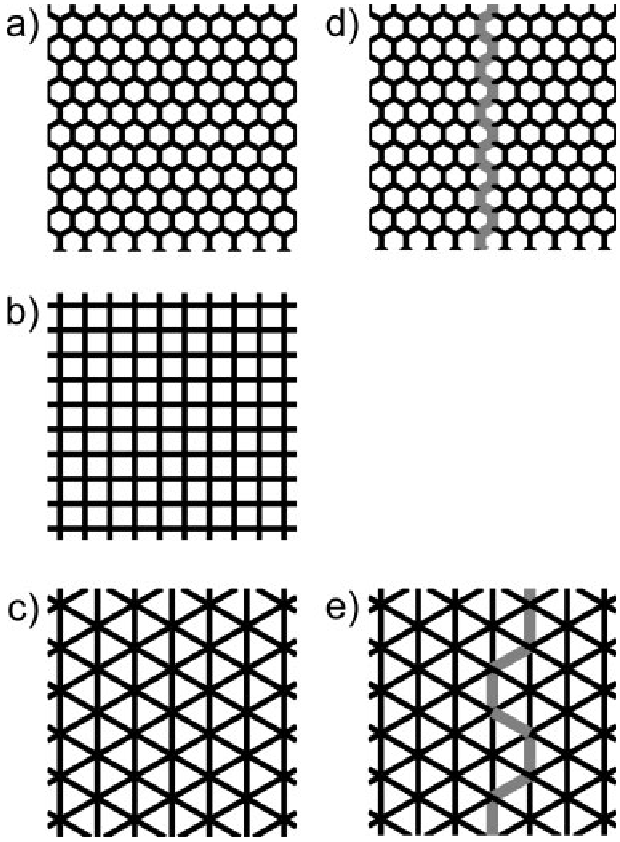

Figure 8. Representations of 2-D networks of different coordination number (a) Z = 3, (b) Z = 4 and (c) Z = 6 with monomodal pore-size distribution, as well as bimodal realizations (d), and (e) with macropore throats in gray.

rate over saturation), believing that they better reveal drying information, and accordingly choose network saturation as a variable to compute distributions of drying rate, as well as average moisture profiles.

In order to plot the distributions of drying rates, as in Figures 6a–c and 9b for the mentioned bimodal and monomodal networks, the following procedure is applied: for a given network saturation (small interval), the Monte-Carlo drying rates are combined to a cumulative frequency distribution. The light gray lines give the envelope of all 100 drying rate curves; the dark gray and black lines show 0.25 levels of the normalized cumulative distributions. (Note that an individual drying curve, as in Figure 5, may be quite different.) Corresponding averaged saturation profiles are plotted against normalized network depth ζ in Figures 7 and 10b.

Drying curves of the first bimodal structure (Figure 6a) show little variation owing to the favorable correlation of pore space; average saturation profiles (Figure 7a) are first getting progressively flatter during the emptying of macrochannels down to a saturation of approximately 0.5, and only then a relatively sharp front recedes.

For the monomodal structure (Figure 10b), and the other bimodal structures (Figures 7b–c), such two distinct periods do not exist. The respective saturation profiles show that, at *local* saturations higher than 0.7, gas can penetrate into the depth of the network at a relatively low gradient, whereas at lower saturations (i.e., at the drying front) a larger saturation gradient is observed. Certainly, the regular pore structure (of the bimodal networks) is reflected in the average saturation profiles: as separated microporous zones in structure 2 (Figure 7b), or as macropores, which have higher probability to empty in structure 3 (Figure 7c). At a larger scale, however, a resemblance between the saturation profiles of bimodal structures 2 and 3, and those of the monomodal structure (Figure 10b) can be stated.

Analyzing drying curve distributions, it can be seen that drying rate decreases rapidly for the monomodal network (Figure 9b). For bimodal structure 3, a small overall enhancement due to the macropores can be noted (e.g., compare drying rates at S = 0.8 in Figures 6c and 9b). Bimodal structure 2 shows a short first drying period (for S < 0.9 in Figure 6b) because of temporarily enhanced capillary flow to network surface. Here, the distribution of drying curves is relatively wide, because the random emptying of a few macrothroats decides on the drying out of whole microporous surface regions (this "amplifying effect" has already been mentioned in the previous section).

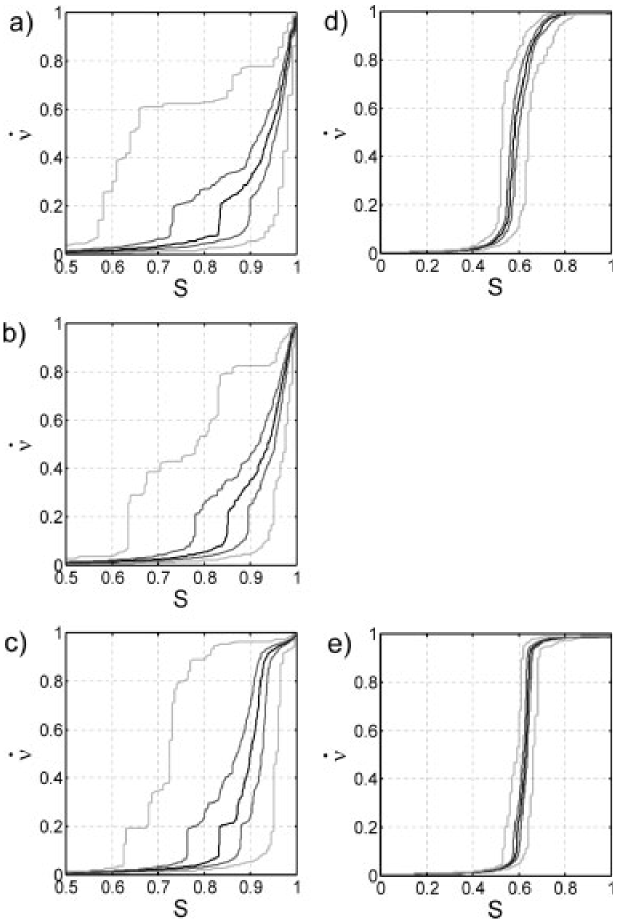

Figure 9. Drying rate curves of the 2-D networks sketched in Figure 8.

Normalized drying rate is plotted vs. network saturation, at 0.25 levels of cumulative distribution for 100 MC runs.

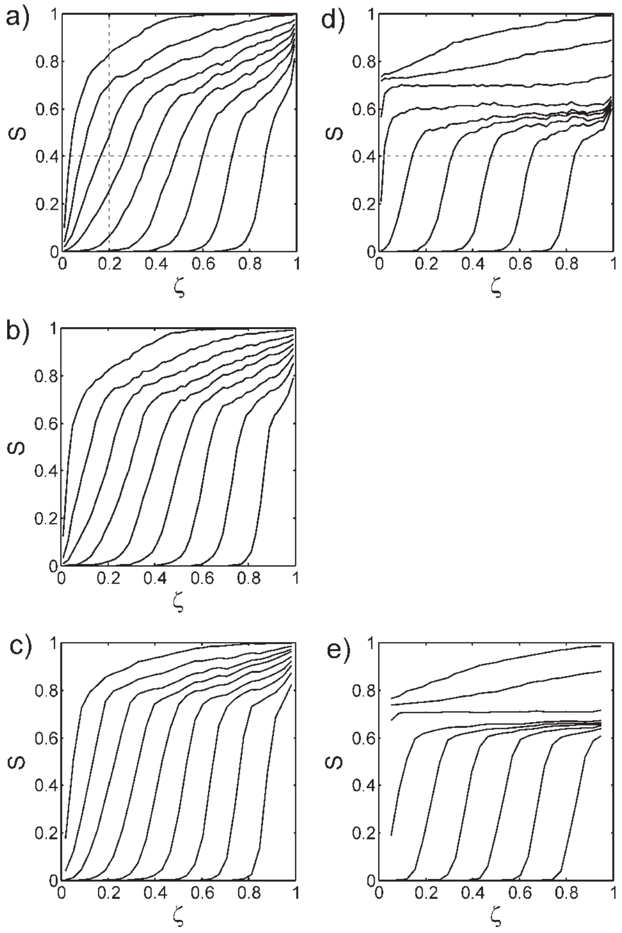

Figure 10. Saturation profiles during drying for the 2-D networks sketched in Figure 8.

Slice-averaged saturation is plotted versus normalized network depth ζ as the average of 100 MC runs, for multiples of 0.1 in network saturation.

Influence of coordination number

After investigating the influence of macrothroats, interconnectivity of pores shall now be varied. Regular monomodal networks of different coordination number Z were generated to this purpose by arranging throats in hexagons and triangles as seen in Figure 8a–c. Care was taken that porosity (defined as throat volume per area) is unchanged, and outer network dimensions are almost the same as for the square network. Consequently, throat length had to be adjusted to 289 μm for Z = 3 (Figure 8a) and 866 μm for Z = 6 (Figure 8c); the networks consist of 8,352 and 2,784 throats, respectively, as compared to 4,800 in the square case. (Radius distribution and drying conditions are unchanged.)

Cumulative distributions of drying curves and average saturation profiles for 100 Monte-Carlo simulations are shown in Figure 9a–c and 10a–c, respectively. Although overall drying behavior has the same features for all three coordination numbers, there are significant quantitative differences. The following trends can be observed: for *lower* Z, initial saturation gradients in the depth of the network are steeper, surface dries out at lower network saturations, and the receding drying front is smoother (compare Figure 10a–c); consequently, drying rate drops more drastically at the beginning (see Figure 9a at $S > 0.9$), but then may stay elevated down to lower saturations ($S < 0.8$).

It is difficult to explain these observations, and at present only possible reasons can be given. Of course, coordination number itself plays a crucial role in terms of liquid connectivity: for each liquid pore, the emptying of the first neighbor throat cuts off capillary flow between the remaining $Z - 1$ liquid throats. Throat length should be of importance as well, since it constitutes the smallest indivisible unit for liquid flow. At last, the very different initial behavior of drying rates for Z = 6 (see Figure 9c at $S > 0.9$) suggests that density, spatial distribution and orientation of throats at the network surface have an influence (confer to Figure 8a–c). In fact, if several throats are connected to a surface node (Figure 8c), this node and its neighborhood are assumed saturated (for discrete modeling of boundary layer), as long as one of the throats contains liquid. Therefore, the fraction of surface, which is considered to be wet, may be higher than the saturation of surface throats. Such surface effects ought to lose importance for a larger network size.

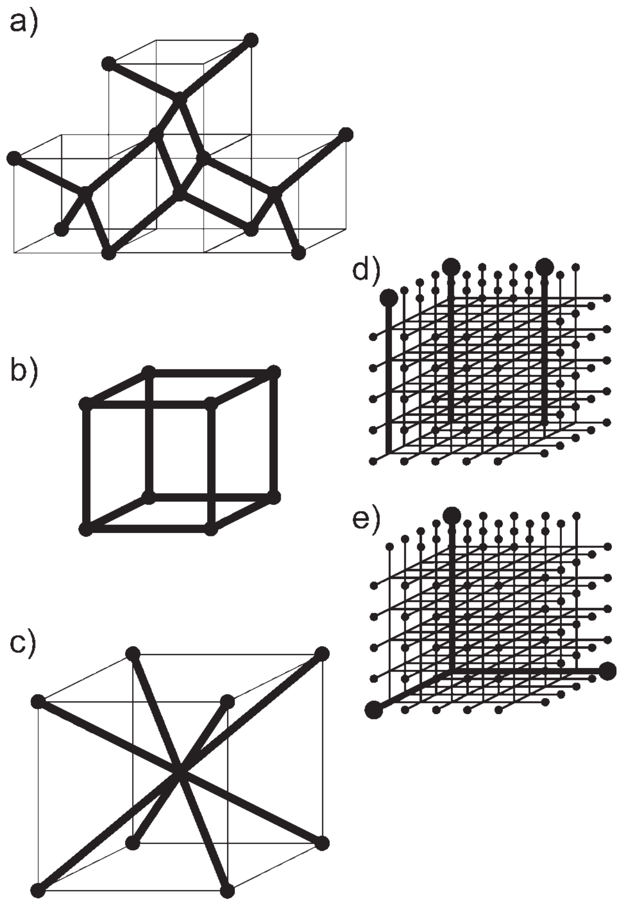

Figure 11. Representations of 3-D network structures of different coordination number (a) Z = 4, (b) Z = 6, and (c) Z = 8, and with macrochannels (d) and (e).

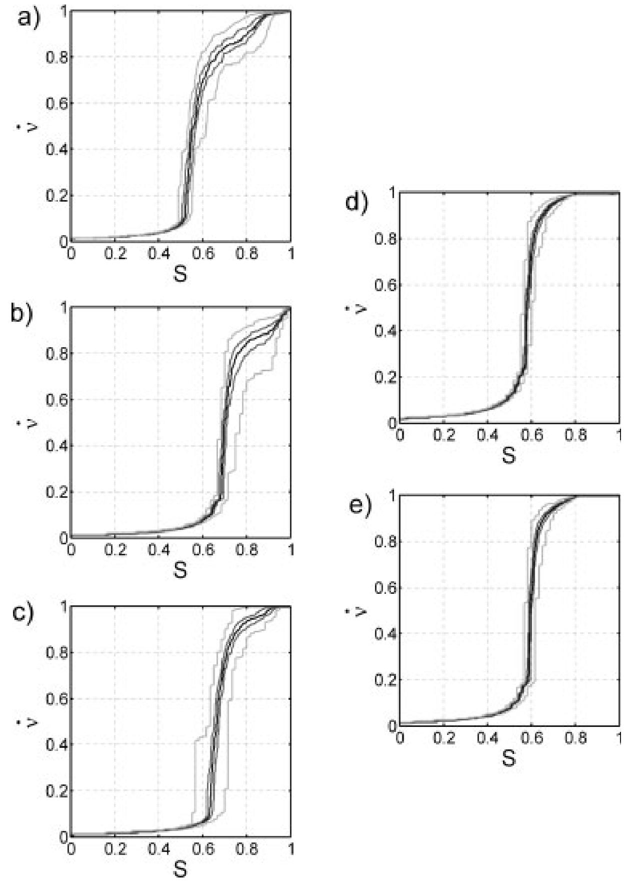

Figure 12. Normalized drying rate vs. network saturation for the 3-D networks as seen in Figure 11 (shown as 0.25 levels of cumulative distribution of MC simulations).

Drying of bimodal networks of coordination numbers Z = 3 and Z = 6 was also simulated; to this purpose, four macro channels (gray in Figure 8d and 8e) were introduced as described previously for Z = 4, in both cases having the same tortuosity and accounting for 0.281 of the total pore volume. A comparison of drying rate curves (Figures 9d–e), as well as saturation profiles (Figures 10d–e) shows that the process becomes dependent on the coordination number only after the macrochannels have emptied, i.e., at S ≈ 0.7. Then, for *low*er Z, the decrease in drying rate starts earlier, but is less steep (Figures 9d and e); and more water can be removed before the evaporation front eventually recedes (for $S < 0.6$ in Figure 10d, for $S > 0.6$ in Figure 10e). The saturation gradient at this front is the same for both cases.

3-D Pore Networks

In this section, the aforementioned investigations are extended to 3-D networks. In three-dimensions, capillary flow paths can more easily be maintained so that a different drying behavior is found.[14] Due to computational limitations, only few 3-D network simulations can be found in literature,[14,15,23] and for large networks, only single network realizations have been investigated.[14,15] In the previous section, we recognized the need for Monte-Carlo simulations; therefore, we choose a network size that allows for a sufficient number of realizations. A periodic cubic 15 × 15 × 16 network (Z = 6), built of 10,125 throats with length 500 μm, serves as reference; for lower coordination number (Z = 4), 16,000 throats of length 329 μm are arranged as tetrahedra; a higher coordination number (Z = 8) is achieved by building octahedra of 8,000 throats (L = 658 μm). All networks have identical porosity (0.060), and approximately the same outer dimensions. To study the influence of a bimodal pore-size distribution, two different arrangements of macrochannels (accounting for a pore-volume fraction of 0.207) are realized for the cubic network. Part of each network is illustrated in Figure 11. For each network, 50 MC simulations were run, except for Z = 4, where only 25 networks were simulated. Drying conditions were chosen as in the 2-D case. Simulation results are again presented as cumulative distributions of all drying rate curves (Figure 12), and averaged saturation profiles (Figure 13).

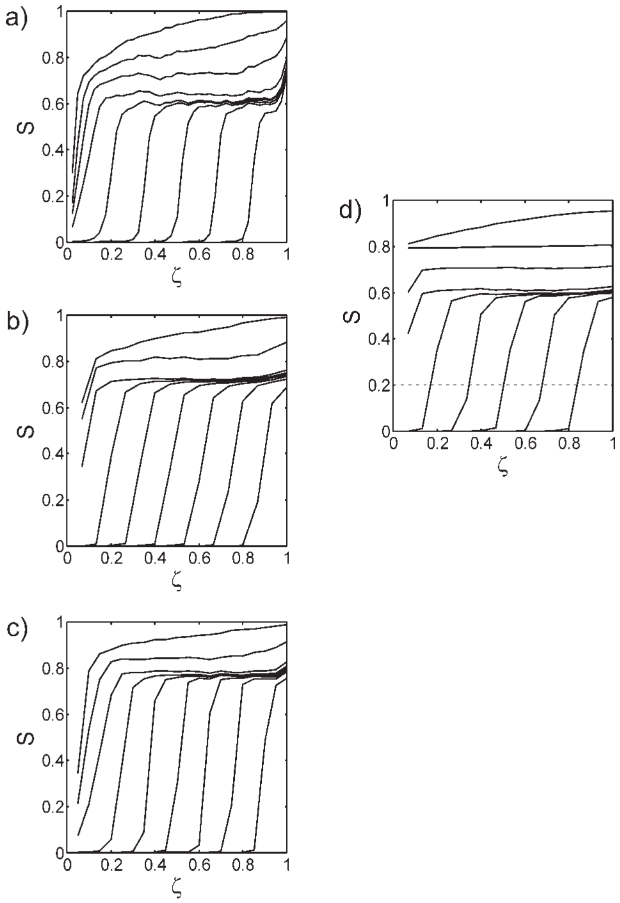

Figure 13. Saturation profiles during drying for 3-D networks of Figure 11; slice-averaged saturation vs. normalized network depth is plotted as the average of MC simulations, for multiples of 0.1 in network saturation.

Influence of coordination number

We start our discussion with the cubic monomodal network (Figures 12b and 13b): a fundamental difference to the 2-D case is that gas can penetrate into the depth of the network, while the so-called main liquid cluster remains connected to network surface, and drying rate stays relatively elevated, although not at the initial value. The formation of disconnected clusters occurs throughout the network at almost uniform saturation, and only then the evaporation front recedes. These characteristics are independent of network size; only the saturation level, at which the front starts to recede, is expected to be lower for larger networks.[14,15]

The saturation profiles (Figure 13b) are similar to those of the bimodal 2-D network with macrochannels perpendicular to network surface (Figure 7a). There, the higher number and ideal spatial distribution of liquid surface throats could produce a true first drying period (see Figure 6a at $S > 0.7$). In contrast, dimensionless drying rate for the 3-D monomodal network drops to $\dot{v} \approx 0.85$ and stays almost constant for $0.95 > S > 0.75$ (Figure 12b); this value of $\dot{v}$ could be raised to unity by increasing boundary-layer thickness.

From the saturation profiles (Figures 13a–c), the following major effect of coordination number can be stated: the *lower* Z, the lower is the saturation level down to which liquid can be removed before the surface dries out completely (as in 2-D). The corresponding drying rate curves (Figures 12a–c) suggest that the surface effects, as discussed in 2-D, play a role in producing higher drying rates and even short first drying periods for the noncubic structures $Z = 4$ and $Z = 8$ (for $S > 0.9$). In three-dimensions, however, surface effects are not expected to disappear with increasing network size, because surface saturation may stay constant during invasion of inner network regions (see discussion later on).

To summarize, we found that, for regular networks of identical porosity, a variation of coordination number has a significant effect on drying behavior. At *lower* coordination number (associated with a shorter throat length), both 2- and 3-D networks could more easily be invaded by the gas (see flatter saturation profiles in Figures 9a–c, and lower saturation level when front recedes in Figure 13a–c). The effect on drying rate is more pronounced in three-dimensions; here, higher rates could be achieved for *lower* coordination number (see Figures 12 a and c).

Influence of pore-size distribution

Based on the 2-D findings, the investigation of bimodal networks is restricted to cubic networks and spatial correlations of macrothroats for which significant changes in drying behavior may be expected. Figures 11d–e show the investigated cases, for both of which liquid-filled microthroats form a continuous phase independent of the filling of macrochannels. Consequently, the drying rate curves in Figures 12d–e show first drying periods ($S > 0.8$) during which all macrothroats are emptied. The orientation of macrochannels has almost no influence on drying rates. Saturation profiles are only plotted for the first case (Figure 13d), because those for the second case have great artifacts due to empty horizontal macrochannels. They show that 40% of liquid can be removed at flat saturation gradients, although only 20% are contained in macrothroats.

Note that for these bimodal networks, like in 2-D, the wet surface spots are more numerous and better spatially distributed than in the monomodal case. In such a way, the presence of macrothroats can enhance drying rates.

Influence of porous medium thickness

In the following, attention is given to network depth; to this purpose, one cubic $15 \times 15 \times 51$ network is generated and decorated with a mono- and bimodal throat radius distribution (as before, see Figures 11b and e). For both structures, drying is first simulated for the entire network, then for the top 31 pore levels, and for the top 16 pore levels. In this way, the surface region remains identical and we can easily investigate the influence of network depth. The results are shown as drying curves in Figure 14, and as saturation profiles for the monomodal case in Figure 15 (network depth z is normalized by throat length L).

Drying behavior of the bimodal structure shows little dependence on network depth. Macrothroats dry out first in any case, and only when the evaporation front recedes, the drying curves diverge because of different distances contributing to mass-transfer resistance (see Figure 14 for $S < 0.6$). Naturally, thinner networks can produce higher drying rates.

The monomodal structure shows initially diverging drying rates if plotted against saturation (see Figure 14 for $S > 0.8$); but if evaporated liquid is used as abscissa, the curves coincide in this region (see circle in inserted figure). In fact, surface saturation only changes up to a critical evaporated mass, before gas penetrates into network depth at constant surface state and drying rate. During this stage, liquid is removed to a uniform level throughout the network ($S \approx 0.75$; see Figure 15) and drying rate curves, as plotted upon saturation (Figure 14), will converge again at that saturation. When the evaporation front recedes, drying curves behave as in the bimodal case.

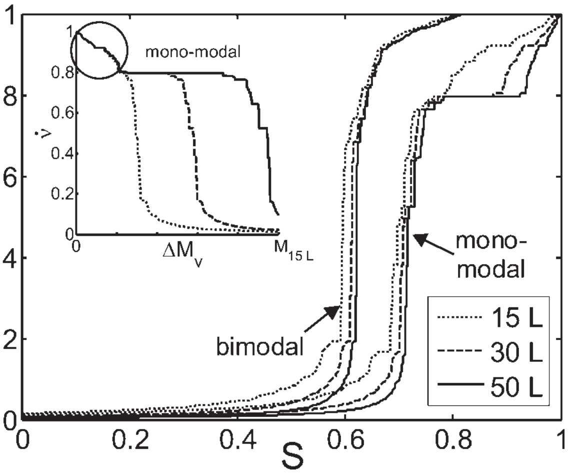

Figure 14. Drying rate curves for the same cubic network with different "active" depth.

Normalized drying rate is plotted vs. network saturation or, in the inserted figure, against mass of evaporated liquid ΔM_v (here, M_{15L} corresponds to the liquid mass contained in the first 15 layers of the network).

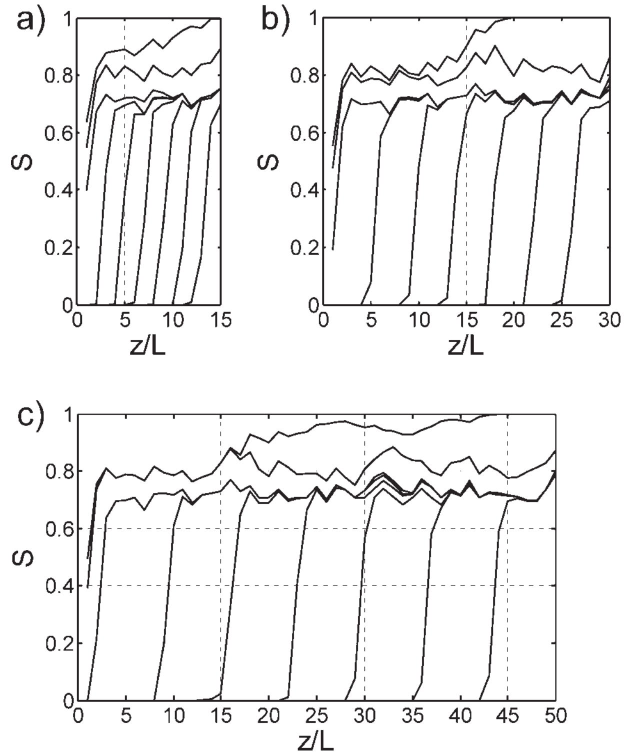

Figure 15. Saturation profiles for the same monomodal cubic network with different "active" depth.

Slice-averaged saturation is plotted vs. dimensionless network depth (for multiples of 0.1 in network saturation).

In conclusion, it may be stated that network depth plays a minor role in the absence of effects that can lead to a stabilization of the drying front, e.g., liquid viscosity.

Influence of boundary layer modeling

At last, we assess the role of lateral vapor transfer in the gas-side boundary layer for the occurrence of a first drying period. Drying of cubic networks (15 × 15 × 16) of mono- and bimodal throat radius distribution is first simulated with the model described in this work; then, lateral vapor diffusion in the boundary layer is suppressed which corresponds to the use of a mass-transfer coefficient (as was common in literature work for a long time). The major effect, shown in Figure 16, is on drying rates, not on phase distributions. A monomodal structure can only maintain a drying rate close to the initial value if the boundary layer allows for lateral mass transfer. Similarly, the first drying period of the bimodal network can be prolonged.

Conclusion

This investigation assumes that a major influence of structure on drying behavior is by capillary effects, and by how the emptying of individual pores affects the continuity of the liquid phase. Other effects like gravity, viscosity or temperature gradients may enhance or more often reduce capillary pumping. Accordingly, a pore network drying model has been used that combines nonviscous capillary flow with diffusive vapor transport. This model has been applied to a range of 2- and 3-D networks representing different pore structures: networks with a monomodal pore-size distribution, and different coordination number and bimodal networks, with different spatial correlations of micro- and macropores. For a good comparison of the drying behavior of different structures, Monte-Carlo simulations were run, and the results plotted as drying curve distributions and averaged saturation profiles.

It was found that pore space connectivity has an influence on drying: networks with lower coordination number (and smaller throat length), showed more favorable drying kinetics. A bigger enhancement effect of capillary pumping can be achieved for bimodal pore size distributions. In this case, microporous regions and macrochannels must form continuous "phases", otherwise, sustained capillary flow from large inner-network pores to small surface pores cannot be guaranteed. This study shows clearly that pore size distribution is no sufficient information but that connectivity and spatial correlations of pore size play an important role.

Furthermore, the role of network depth has been investigated. It was found that in the absence of gradients (due to gravity, liquid viscosity or heat transfer), which could stabilize or destabilize the drying front, network depth has little effect on drying behavior. Only at lower saturations, when the evaporation front starts to recede, thicker networks have lower drying rates due to a higher overall mass-transfer resistance. At last, different model versions for mass transfer through the gas-side boundary layer have been compared; here, the importance of lateral vapor transfer for a constant drying period has been pointed out.

Further investigations are recommended in the context of pore connectivity to better understand the influence of throat length as well as the role of density and orientation of surface throats. Certainly, the presented approach can easily be extended to pore networks with random pore node locations, randomly established throat connections and random spatial correlations of throat radius.

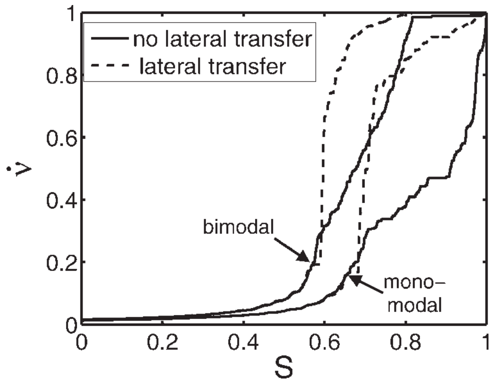

Figure 16. Drying rate curves for cubic networks with and without lateral transfer in boundary layer.

Normalized drying rate is plotted vs. network saturation for mono- and bimodal network.

This work confirms how pore network models allow investigating transport phenomena in porous media at a more fundamental level than continuous models with effective parameters. Specifically, they are an ideal tool to study the influence of structural effects on the process. Their physical significance has been proven at the laboratory scale, e.g., in drying.[12] At present, the amount of data needed for simulating real porous media and computational time are limiting so that pore network studies are still qualitative. Nevertheless, such studies can help to identify favorable pore structures, such as for drying in this work. By their fundamental nature, pore networks are a versatile tool and can be applied to many other processes of practical relevance, such as chemical reactions in porous catalysts,[31] helping to improve product quality for specialized applications in many fields.

Acknowledgments

The first author would like to thank the German Research Foundation (DFG) which financed the contributions by the second author in the frame of Graduate School 828 "Micro-Macro-Interactions in Structured Media and Particle Systems".

Literature Cited

1. Perré P, Turner IW. A 3-D version of TransPore: a comprehensive heat and mass transfer computational model for simulating the drying of porous media. *Int J Heat Mass Transfer.* 1999;42:4501–4521.
2. Metzger T, Tsotsas E. Influence of pore size distribution on drying kinetics: a simple capillary model. *Drying Technol.* 2005;23:1797–1809.
3. Vu TH. Influence of pore size distribution on drying behaviour of porous media by a continuous model. Otto-von-Guericke-University, Magdeburg; 2006. PhD thesis.
4. Vu TH, Metzger T, Tsotsas E. Influence of pore size distribution via effective parameters in a continuous drying model. Proceedings 15th Intern. Drying Symposium. Budapest, Hungary, August 20-23, 2006:B 554–560.
5. Nowicki SC, Davis HT, Scriven LE. Microscopic determination of transport parameters in drying porous media. *Drying Technol.* 1992;10:925–946.
6. Prat M. Percolation model of drying under isothermal conditions in porous media. *Int J Multiphase Flow.* 1993;19:691–704.
7. Irawan A. Isothermal drying of pore networks: influence of pore structure on drying kinetics. Otto-von-Guericke-University, Magdeburg; 2006. PhD thesis.
8. Metzger T, Irawan A, Tsotsas E. Isothermal drying of pore networks: Influence of friction for different pore structures. *Drying Technol.* 2007;25:49–57.
9. Yiotis AG, Stubos AK, Boudouvis AG, Yortsos YC. A 2-D pore-network model of the drying of single-component liquids in porous media. *Adv Water Resour.* 2001;24:439–460.
10. Yiotis AG, Boudouvis AG, Stubos AK, Tsimpanogiannis IN, Yortsos YC. The effect of liquid films on the drying of porous media. *AIChE J.* 2004;50:2721–2737.
11. Prat M. On the influence of pore shape, contact angle and film flows on drying of capillary porous media. *Int J Heat Mass Transfer.* 2007;50:1455–1468.
12. Laurindo JB, Prat M. Numerical and experimental network study of evaporation in capillary porous media, phase distributions. *Chem Eng Sci.* 1996;51:5171–5185.
13. Laurindo JB, Prat M. Numerical and experimental network study of evaporation in capillary porous media, drying rates. *Chem Eng Sci.* 1998;53:2257–2269.
14. Le Bray Y, Prat M. Three dimensional pore network simulation of drying in capillary porous media. *Int J Heat Mass Transfer.* 1999; 42:4207–4224.
15. Yiotis AG, Tsimpanogiannis IN, Stubos AK, Yortsos YC. Pore-network study of the characteristic periods in the drying of porous materials. *J Colloid Interface Sci.* 2006;297:738–748.
16. Irawan A, Metzger T, Tsotsas E. Pore network modeling of drying: combination with a boundary layer model to capture the first drying period. 7th World Congress of Chemical Engineering. Glasgow, Scotland; July 10–14, 2005:P42–033.
17. de Freitas DS, Prat M. Pore network simulation of evaporation of a binary liquid from a capillary porous medium. *Transport in Porous Media.* 2000;40:1–25.
18. Huinink HP, Pel L, Michels MAJ, Prat M. Drying processes in the presence of temperature gradients, pore-scale modeling. *Eur Physical J E.* 2002;9:487–498.
19. Plourde F, Prat M. Pore network simulations of drying of capillary media, influence of thermal gradients. *Int J Heat Mass Transfer.* 2003;46:1293–1307.
20. Surasani VK, Metzger T, Tsotsas E. Consideration of heat transfer in pore network modelling of convective drying. doi: 10.1016/j.ijheatmasstransfer. 2007.07.033. *Int J Heat Mass Transfer*.
21. Tsimpanogiannis IN, Yortsos YC, Poulou S, Kanellopoulos N, Stubos AK. Scaling theory of drying in porous media. *Phys Rev E.* 1999;59:4353–4365.
22. Prat M, Bouleux F. Drying of capillary porous media with stabilized front in two dimensions. *Phys Rev E.* 1999;60:5647–5656.
23. Segura LA, Toledo PG. Pore-level modeling of isothermal drying of pore networks, effects of gravity and pore shape and size distributions on saturation and transport parameters. *Chem Eng J.* 2005; 111:237–252.
24. Metzger T, Irawan A, Tsotsas E. Discrete modeling of drying kinetics of porous media. Proceedings 3rd Nordic Drying Conference. Karlstad, Sweden, June 15-17, 2005.
25. Laurindo JB, Prat M. Modeling of drying of capillary porous media, the discrete approach. *Drying Technol.* 1998;16:1769–1787.
26. Metzger T, Tsotsas E, Prat M. Chapter 2: Pore network models. In: Tsotsas E, Mujumdar AS, eds. *Modern Drying Technology 1: Computational Tools at Differents Scales*. John Wiley & Sons, 2007, pp. 57–102.
27. Schlünder EU. On the mechanism of the constant drying rate period and its relevance to diffusion controlled catalytic gas phase reactions. *Chem. Eng. Sci.* 1988;43:2685–2688.
28. Al-Futaisi A, Patzek TW. Extension of Hoshen-Kopelman algorithm to non-lattice environments. *Physica A.* 2003;321:665–678.
29. Metzger T, Irawan A, Tsotsas E. Remarks on the paper Extension of Hoshen-Kopelman algorithm to non-lattice environments: by Al-Futaisi A, Patzek TW. *Physica A.* 2003;321:665–678. *Physica A.* 2006; 363:558–560.
30. Chapuis O, Prat M. Influence of wettability conditions on slow evaporation in two-dimensional porous media. *Physical Review E.* 2007; 75: article no. 046311.
31. Wood J, Gladden LF, Keil F. Modelling diffusion and reaction accompanied with capillary condensation using three-dimensional pore networks, part 2: dusty gas model and general reaction kinetics. *Chem Eng Sci.* 2002;57:3047–3059.

Manuscript received Apr. 17, 2007, and revision received Aug. 7, 2007.